JCTC Journal of Chemical Theory and Computation

pubs.acs.org/JCTC Article

CHARMM-GUI Nanomaterial Modeler for Modeling and Simulation of Nanomaterial Systems

Yeol Kyo Choi,[#] Nathan R. Kern,[#] Seonghan Kim,[#] Krishan Kanhaiya, Yaser Afshar, Sun Hee Jeon, Sunhwan Jo, Bernard R. Brooks, Jumin Lee, Ellad B. Tadmor, Hendrik Heinz, and Wonpil Im*

Cite This: *J. Chem. Theory Comput.* 2022, 18, 479−493 Read Online

ACCESS | Metrics & More | Article Recommendations | Supporting Information

ABSTRACT: Molecular modeling and simulation are invaluable tools for nanoscience that predict mechanical, physicochemical, and thermodynamic properties of nanomaterials and provide molecular-level insight into underlying mechanisms. However, building nanomaterial-containing systems remains challenging due to the lack of reliable and integrated cyberinfrastructures. Here we present Nanomaterial Modeler in CHARMM-GUI, a web-based cyberinfrastructure that provides an automated process to generate various nanomaterial models, associated topologies, and configuration files to perform state-of-the-art molecular dynamics simulations using most simulation packages. The nanomaterial models are based on the interface force field, one of the most reliable force fields (FFs). The transferability of nanomaterial models among the simulation programs was assessed by single-point energy calculations, which yielded 0.01% relative absolute energy differences for various surface models and equilibrium nanoparticle shapes. Three widely used Lennard-Jones (LJ) cutoff methods are employed to evaluate the compatibility of nanomaterial models with respect to conventional biomolecular FFs: simple truncation at r = 12 Å (12 cutoff), force-based switching over 10 to 12 Å (10−12 fsw), and LJ particle mesh Ewald with no cutoff (LJPME). The FF parameters with these LJ cutoff methods are extensively validated by reproducing structural, interfacial, and mechanical properties. We find that the computed density and surface energies are in good agreement with reported experimental results, although the simulation results increase in the following order: 10−12 fsw <12 cutoff < LJPME. Nanomaterials in which LJ interactions are a major component show relatively higher deviations (up to 4% in density and 8% in surface energy differences) compared with the experiment. Nanomaterial Modeler's capability is also demonstrated by generating complex systems of nanomaterial−biomolecule and nanomaterial−polymer interfaces with a combination of existing CHARMM-GUI modules. We hope that Nanomaterial Modeler can be used to carry out innovative nanomaterial modeling and simulations to acquire insight into the structure, dynamics, and underlying mechanisms of complex nanomaterial-containing systems.

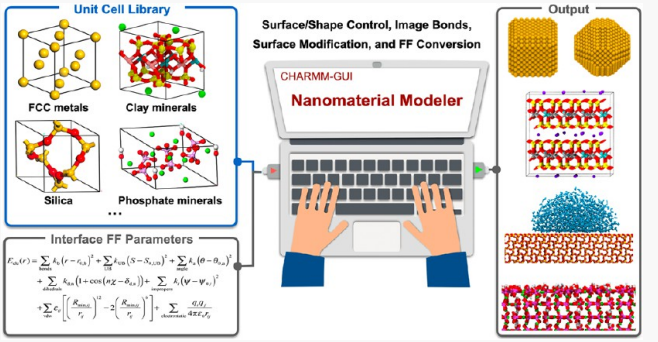

1. INTRODUCTION

Understanding the dynamical evolution of biological and materials systems on the atomic scale is essential for groundbreaking advances in health science, materials science, energy conversion, sustainability, and overall quality of life.[1−5] However, progress is limited because current experimental techniques alone cannot provide complete information about structures and dynamical processes on the nanometer to micrometer scale. Classical molecular modeling and simulation using force fields (FFs) and complex configuration databases are playing an increasingly important role in explaining experimental data, elucidating design principles, and making transformative property predictions for unknown biomolecular and nanomaterial structures and dynamics as well as their interfaces. These computational methods are suitable for harnessing big data and accelerating discovery from the quantum scale to the microscale.[6−8]

State-of-the-art FFs for biomolecular systems (e.g., proteins, lipids, nucleic acids, and carbohydrates) have matured to the point where they can explain experiments and accelerate the experimental discovery via testable hypotheses.[9,10] The same is true for the growing number of surface models for nanomaterials and nanomaterial−biological (nanobio) interfaces.[11,12] In particular, the surface model database and parameters for metals, clay minerals, silica, apatites, layered materials (e.g., MoS_2 and graphite), cement minerals, and gas molecules in the interface force field[11] (IFF) routinely achieve more accurate

Received: October 4, 2021
Published: December 6, 2021

Table 1. Nanomaterials Available in Nanomaterial Modeler and Corresponding References

class	material (chemical formula)	shape	remarks
fcc metals	Ac, Ag, Al, Au, Ca (α), Ce (γ), Cu, Es (β), Fe (γ), Ir, Ni, Pb, Pd, Pt, Rh, Sr (α), Th (α), and Yb (β)	box,[a] cylinder, rod, polygon, sphere, Wulff	refs 38 and 39
clay minerals	pyrophyllite ($Al_2Si_4O_{10}(OH)_2$)	box	ref 40
	kaolinite ($Al_2Si_2O_5(OH)_4$)	box	ref 40
	montmorillonite ($(K, Na)_n[Si_4O_8][Al_{2-n}Mg_nO_2(OH)_2]$)	box	ref 40
	muscovite ($KAl_2(AlSi_3)O_{10}(OH)_2$)	box	ref 40
calcium sulfates	gypsum ($CaSO_4{\cdot}2H_2O$)	box, Wulff	ref 13
	hemihydrate ($CaSO_4{\cdot}1/2H_2O$)	box	ref 13
	anhydrite ($CaSO_4$)	box	ref 13
cement minerals	tricalcium silicate (Ca_3SiO_5)	box, Wulff	ref 41
	tricalcium aluminate ($Ca_3Al_2O_6$)	box	ref 42
calcium silicate hydrate	tobermorite ($Ca_4Si_6O_{15}(OH)_2{\cdot}5H_2O$)	box	ref 42
silica	α-quartz (SiO_2)	box, sphere	ref 43
	α-cristobalite (SiO_2)	box, sphere	ref 43
phosphate minerals	hydroxyapatite ($Ca_5(PO_4)_3(OH)$)	box, Wulff	ref 44
transition metal dichalcogenides	molybdenum (MoS_2)	box	ref 15
carbonaceous materials	carbon nanotube		ref 45
	graphene	box, hexagonal	ref 45
	graphite	box	ref 45

[a]Box represents a rectangular parallelepiped shape.

predictions of surface energies, binding energies, and molecular recognition than typical density functional theory (DFT) methods and are compatible with biomolecular FFs.[13−15] These recent developments present a unique opportunity for the life and material sciences to harness the predictive power of computer simulation methods to explore a broad range of nanobio interfaces and complex electrolytes.

A recent round-robin study showed that distinct user groups working with different simulation FFs and programs yielded inconsistent results even for calculating simple thermodynamic properties such as density and potential energy.[16] The lack of a reliable and unified cyberinfrastructure to build complex nanobio interfaces poses major challenges to the molecular modeling and simulation community in terms of steep learning curves, risks of choosing unsuitable FF and faulty interface models, and mistakes in file conversion and input scripts that render simulations less useful or invalid. Several programs have been developed to help users to build nanomaterial model systems, including web applications, such as NanoModeler[17] and PubVINAS,[18] and stand-alone software packages, such as Atomic Simulation Environment (ASE),[19] pysimm,[20] Molecular Simulation Design Framework (MoSDeF),[21] and NanoMaterialCAD.[22] NanoModeler supports 16 gold nanocluster models with ligand grafting function, and PubVINAS provides 11 material types with corresponding physicochemical properties or bioactivities. ASE, pysimm, and MoSDeF provide methods for preparing various nanomaterial systems and application programming interfaces (APIs) to integrate different features of existing software packages using Python-based scripting. NanoMaterialsCAD offers a graphical user interface (GUI) to build and manipulate a nanomaterial system. However, all of the aforementioned software require significant preprocessing to prepare structures, topologies, and parameters of nanomaterials for simulation or are limited to using specific prebuilt nanostructures. Commercial packages also exist, such as Material Studio,[23] Schrödinger,[24] and Amsterdam Modeling Suite,[25] but are not freely available to everyone. Furthermore, the models from these programs are not transferable to other molecular dynamics (MD) simulation packages. Therefore, building models of functional nanobio materials such as nanoparticle therapeutics, imaging agents, biomineral structures, bioinspired composites, and biosensors has been challenging to accomplish. Moreover, the simulation input preparation for nanomaterials and nanobio interfaces currently involves multiple operations by researchers. This process includes the choice of building tools or scripts and file conversion and reassignment of FF parameters depending on the chosen simulation platform. Unfortunately, no single, user-friendly cyberinfrastructure is available to accomplish these crucial tasks.

CHARMM-GUI (https://www.charmm-gui.org), a web-based GUI, provides a well-designed workflow to interactively construct various complex biomolecular systems and seamlessly handles complicated internal data structures and simulation input files for CHARMM,[26] NAMD,[27] GROMACS,[28] AMBER,[29] GENESIS,[30] LAMMPS,[31] TINKER,[32] Desmond,[33] and OpenMM[34] with several biomolecular FFs.[7] The simulation protocols are optimized[6] following the principles of the original FF development.[35,36] Therefore, CHARMM-GUI is widely utilized in studies on the role of biomolecular motions, conformational changes, and thermodynamic relationships in biological function.

This work presents Nanomaterial Modeler, an important extension of CHARMM-GUI to a broad range of nanomaterials based on the IFF, which can bridge the gap between biomolecular and material simulations through compatibility with multiple simulation platforms.[8,37] Nanomaterial Modeler enables researchers to build nanomaterials models with up to 5 000 000 atoms and addresses the aforementioned needs by merging the IFF and CHARMM-GUI in an easy-to-use and state-of-the-art platform. The following sections discuss the methods, workflow, available nanomaterials models, user interface, supported simulation engines, validation of the models, and example applications. The article ends with brief conclusions.

https://doi.org/10.1021/acs.jctc.1c00996
J. Chem. Theory Comput. 2022, 18, 479−493

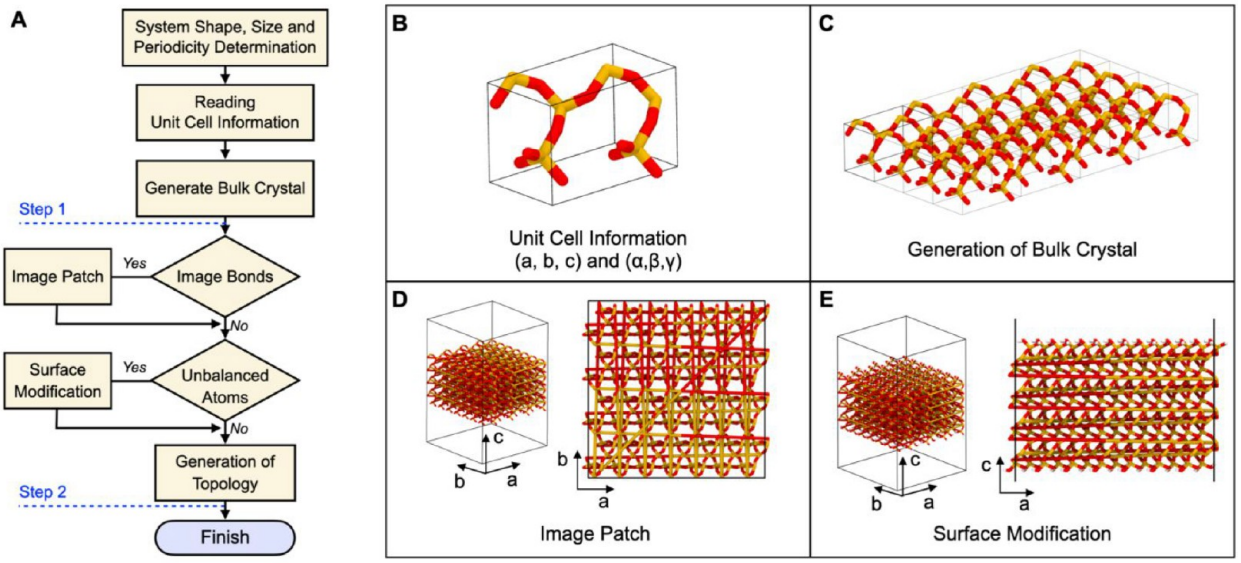

Figure 1. Illustration of the Nanomaterial Modeler workflow. (A) Workflow of Nanomaterial Modeler. (B) Unit cell information is used to build nanomaterials. (C) Each unit cell structure is duplicated and translated for the generation of the user-specified system size. (D) For systems having bonds along a specific direction, bond linkages across the neighboring periodic images are built. (E) Surface modification is performed to facilitate hydrogenation and ionization.

2. METHODS

2.1. Workflow of Nanomaterial Modeler. Currently, CHARMM-GUI Nanomaterial Modeler supports 10 classes of nanomaterials, including fcc metals, clay minerals, calcium sulfates, cement minerals, calcium silicate hydrate, silica, phosphate minerals, transition metal dichalcogenides (TMDCs), and carbonaceous materials (Table 1).

Figure 1A shows an overall nanomaterial-system-building process that has been generalized and automated in two subsequent steps. Each step is designed to incorporate user's specific options through a web interface and run CHARMM input files. Individual input and output files, including the generated structure and an archive of all created files, are available at each step. Video demonstrations on how to use Nanomaterial Modeler are available on the CHARMM-GUI website (http://www.charmm-gui.org/demo/nanomaterial). Nanomaterial Modeler adopts a GUI that allows researchers to quickly check and design nanomaterials (i.e., size and shape of nanomaterials, chemical modification of the surface, and periodicity along each axis).

Step 1: Building bulk crystal(s). In step 1, users can set the material type, shape, Miller index, size, and periodicity along the *X*, *Y*, and *Z* directions. A unit-cell structure of a selected nanomaterial (Figure 1B) is used to generate a user-specified nanomaterial system through unit-cell duplication and translation (Figure 1C).

Step 2: Treatment of unbalanced atoms and surface modification. For specific nanomaterials, bonds between the primary and neighboring cells (i.e., image bonds) are required to model an infinite surface or molecule along with the periodic images. The "patch information" necessary to create such connections has been defined for the currently supported nanomaterials to facilitate such image bonds (Figure 1D). The patch information includes all bonds, angles, dihedrals, and partial charge and atomic type information that are created when the primary cell connects to the 26 image cells. After the periodicity is set, Nanomaterial Modeler performs the necessary surface ionization, defect generation, or surface chemical modification (Figure 1E). At the end, researchers can obtain a nanomaterial system with the desired structure, topology, FF parameters, and simulation configuration files for further simulation. Furthermore, the generated structure can be used in CHARMM-GUI Multicomponent Assembler to model nanobio systems (see the Supporting Information and Section 3.6).

Nanomaterial Modeler provides validated all-atom simulation inputs for various MD programs, including CHARMM, GROMACS, NAMD, LAMMPS, AMBER, GENESIS, and OpenMM, enabling researchers to employ the package of their choice. (See the Supporting Information, Tables S1 and S2.) In the original IFF, electrostatic interactions are calculated using the particle mesh Ewald (PME) method, and two Lennard-Jones (LJ) potentials (i.e., the 12-6 and 9-6 forms) are adapted. Nanomaterial Modeler supports a 12-6 LJ potential because the conventional biomolecular FFs such as AMBER,[46] CHARMM,[47−49] GROMOS,[50] and OPLS-AA[51] have been developed with a 12-6 LJ potential

$$V_{LJ}(r) = 4\varepsilon[(\sigma/r)^{12} - (\sigma/r)^{6}]$$

where r is the distance between two interacting particles, ε is the depth of the potential well, and σ represents the distance at which the particle−particle potential energy is zero. In practice, the V_{LJ} interactions are negligible at large distances, so that an energy cutoff is introduced at a certain interparticle distance. A 12 Å cutoff is chosen for the IFF due to the rapid loss of the electron−electron correlation of London dispersion interactions with distance after a few layers of nearest neighbors, in contrast with long-range Coulomb interactions between permanently charged atoms.[52,53] While a 12 Å cutoff is generally accepted for various FFs, different cutoff methods have been used in conventional biomolecular FFs for different FF forms. The most widely used methods are (i) simple truncation at r = 12 Å (12 cutoff), (ii) force-based switching over 10 to 12 Å (10−12 fsw[54]), and (iii) LJ particle mesh Ewald (LJPME). Single-point energy calculations of hydroxyapatite and α-quartz were performed to compare the

https://doi.org/10.1021/acs.jctc.1c00996
J. Chem. Theory Comput. 2022, 18, 479−493

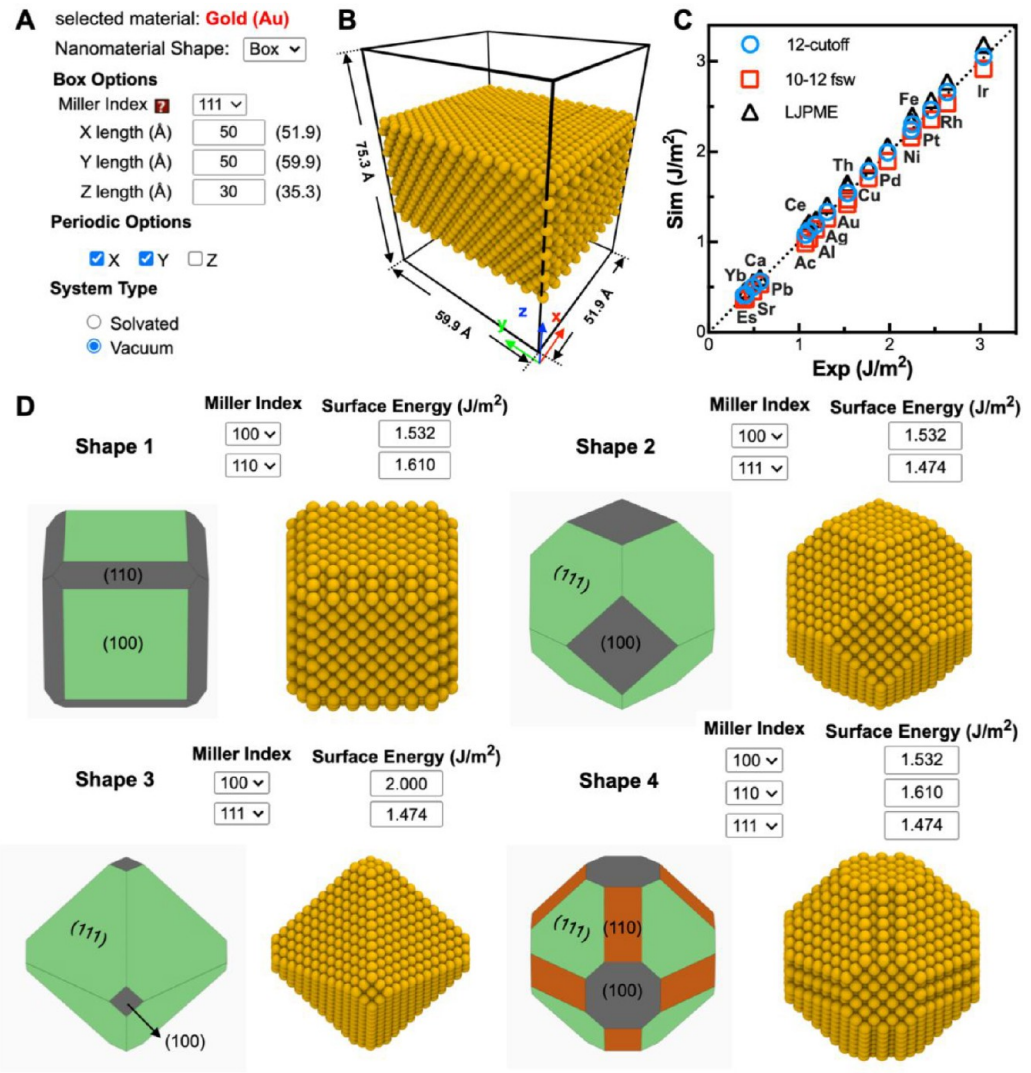

Figure 2. Building surfaces and equilibrium shapes of gold nanoparticles using Nanomaterial Modeler. (A) User interface of Nanomaterial Modeler for building a (111) gold surface. One can select X, Y, and Z under "Periodic Options" to define the periodicity of the gold surface along each axis and choose a "System Type" to build the nanomaterial in water or in vacuum. (B) All-atom model obtained from the options in panel A. (C) Comparison of simulated and experimental surface energies of 18 fcc metals for (111) surfaces. Three LJ cutoff methods (i.e., 12 Å cutoff, 10−12 Å fsw, and LJPME) were used to calculate surface energies. (D) Predicted equilibrium shapes using Wulff construction and corresponding all-atom models of gold nanoparticles. The shape depends on a combination of Miller indices and the corresponding surface energies.

implementations of all supported MD programs and LJ methods (Table S3). The results show that all simulation programs are in excellent agreement with a maximum difference of 0.01% in total energy, indicating that the nanomaterial IFF is correctly implemented within CHARMM-GUI. Note that the small differences are inevitable due to the usage of slightly different conversion factors within the programs and the 10−12 fsw function implemented in GROMACS, which is slightly different with other software.[55] In this work, the mechanical, physicochemical, and thermodynamic properties are analyzed using these LJ cutoff methods to assess the transferability of the IFF for different simulation packages and the ability to model complex nanobio systems in combination with various biomolecular FFs.

2.2. Model Building. The unit-cell structures of all nanomaterials are obtained from X-ray diffraction data[56−58] and the IFF database.[8] Starting from the conventional unit cell, a series of lattice vector transformations are performed to create an "oriented" unit cell (OUC) where the *a* and *b* lattice vectors are parallel to the plane with Miller indices (*hkl*).[59] Note that the *c* lattice vector is not necessarily perpendicular to the plane, although an orthogonal vector obtained within a reasonable cell size is used. For example, 18 fcc metals with 13 Miller indices have $\alpha = \beta = \gamma = 90°$. All lattice parameters of the OUC of supported nanomaterials are summarized in Tables S4 and S5. Model building methods for larger models from multiple unit cells are described in Figure 1. All model building procedures are controlled by CHARMM scripts, and individual input and output files, including the CHARMM scripts and an archive of all created files (i.e., structure, topology, and configuration files), are available on the Nanomaterial Modeler website (http://charmm-gui.org/input/nanomaterial). Details of the complex nanobio and nanopolymer system building are summarized in Supporting Information.

2.3. Computational Details. All simulations used the IFF for nanomaterials, the CHARMM FF for proteins, peptides, and lipids, and the CHARMM generalized FF for poly-

https://doi.org/10.1021/acs.jctc.1c00996
J. Chem. Theory Comput. 2022, 18, 479−493

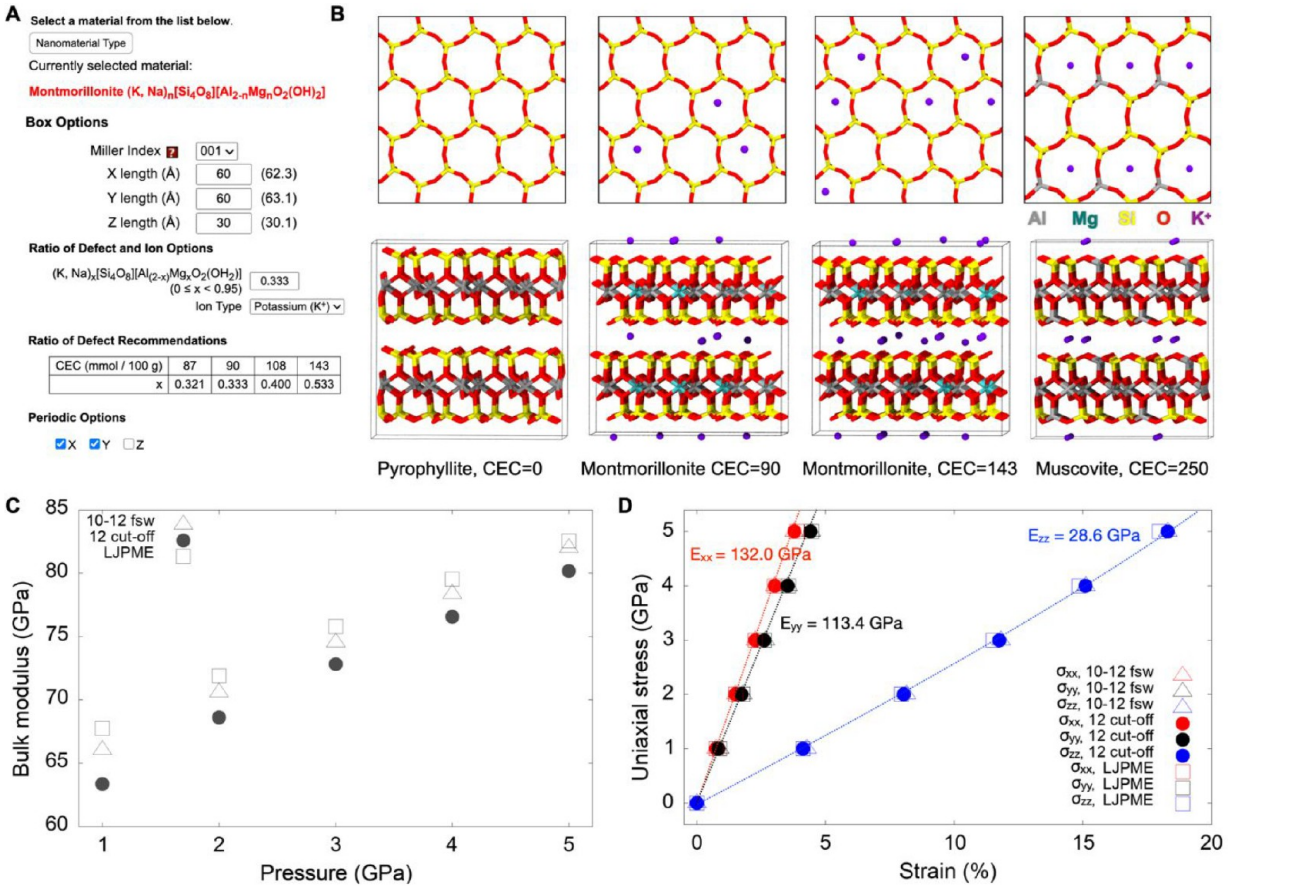

Figure 3. (A) User interface to generate 0.333 mmol/100g cation exchange capacity (CEC) montmorillonite. (B) Illustrative snapshots of top (upper panel) and side (lower panel) views of pyrophyllite, montmorillonite, and muscovite. In the top view, the layers located below the top layer are hidden to show the different CEC states clearly. (C) Bulk modulus of muscovite with different LJ cutoff methods as a function of applied pressure. (D) Young's modulus of muscovite along the *X*, *Y*, and *Z* directions with different LJ methods. Error bars are smaller than the symbol size. Aluminum, magnesium, silicon, oxygen, and potassium ions are colored in gray, green, yellow, red, and purple, respectively.

mers.[9,36,60] The TIP3P water model was utilized for water-containing systems. Three independent molecular dynamics (MD) simulations were performed for each system to achieve better sampling and check convergence. Periodic boundary conditions (PBCs) were employed for all simulations, and the PME method[61] was used for long-range electrostatic interactions. A leapfrog algorithm was used to integrate Newton's equation of motion. The simulation time step was set to 1 fs for equilibration and 2 fs for the production run in conjunction with the SHAKE algorithm[62] to constrain the covalent bonds involving hydrogen atoms for all programs except GROMACS, in which the LINCS algorithm[63] was used instead. All simulation trajectories were recorded every 10 ps, except for the vibrational frequency calculation. (See the Supporting Information.) For each nanomaterial model, all structure and corresponding parameter files were generated in the CHARMM format (i.e., rtf and prm files). For GROMACS, Amber, and LAMMPS, FF-Converter in CHARMM-GUI[64] was used for format conversion from CHARMM data format to corresponding program readable formats. For specific nanomaterials, bonds between the primary and neighboring cells (image-bond) are required to model infinite surfaces or molecules along with the periodic images. Nanomaterial Modeler supports CHARMM, NAMD, GROMACS, LAMMPS, OpenMM, Amber, and Genesis for non-image-bond systems such as fcc metals. Four simulation programs, OpenMM, Gromacs, LAMMPS, and NAMD, support image-bond systems. Three types of LJ cutoff methods, including 10−12 fsw, 12 cutoff, and LJPME, were employed for the LJ interactions to investigate the cutoff method effect on the structural, physical, and mechanical properties. For LJPME, the grid spacing and interpolation order were set to 1.2 Å and 4, respectively. Details of the computational methods such as the thermostat, barostat, and coupling constants for each simulation program are described in Supporting Information S1. Computational details of the density, surface energies, mechanical properties, and the vibrational spectra calculation for various nanomaterials are provided in Supporting Information S2−S7.

3. RESULTS AND DISCUSSION

3.1. Metals: Gold Surfaces with Various Miller Indices and Their Equilibrium Particle Shapes. Nanomaterial Modeler supports 18 fcc metals (Table 1): Ac, Ag, Al, Au, Ca (α), Ce (γ), Cu, Es (β), Fe (γ), Ir, Ni, Pb, Pd, Pt, Rh, Sr (α), Th (α), and Yb (β). One can generate (i) bulk crystal, (ii) different cleavage surfaces with Miller indices ranging from (100) to (332) with any combination of periodicity, and (iii) a variety of shapes such as sphere, cylinder, rod, polygon, box, and Wulff construction. Figure 2A shows the user interface of Nanomaterial Modeler for building a (111) gold surface with a size of 51.9 × 59.9 × 35.3 Å^3; note that the input dimension

https://doi.org/10.1021/acs.jctc.1c00996
J. Chem. Theory Comput. 2022, 18, 479−493

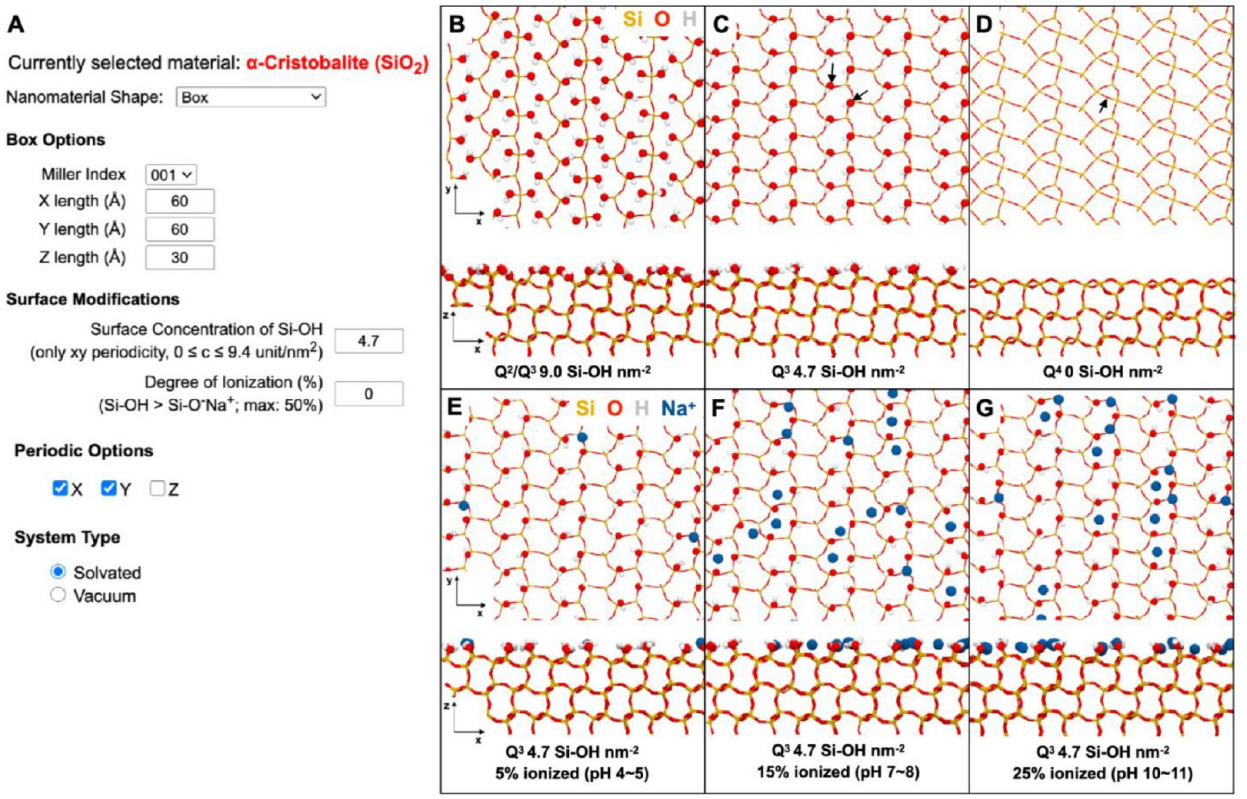

Figure 4. Generation of silica surface models using Nanomaterial Modeler. (A) User interface to build a (20−2) α-cristobalite surface with a size of 60 × 60 × 30 Å^3. (B−D) Q^2/Q^3, Q^3, and Q^4 surfaces with a total Si−OH density of 9.0, 4.7, and 0 nm^{-2} with top (upper panel) and side views (lower panel). Black arrows indicate the formation of siloxide bridges from two silanol groups. (E−G) Q^3 surfaces with a total Si−O(H, Na) density of 4.7 nm^{-2} and 5, 15, and 25% ionization with top (upper panel) and side (lower panel) views. Silica, oxygen, hydrogen, and sodium are colored in yellow, red, gray, and blue, respectively.

and the final model dimension can be different because of the unit cell size. The selected (111) Miller index plane is perpendicular to the Z axis. With user-specified X, Y, and Z dimensions, Nanomaterial Modeler displays an estimated system size from the unit-cell information. (See the Supporting Information for the lattice parameters of all unit cells.) Periodicity can be selected in the X and Y directions and vacuum can be selected under "System Type" to build an infinite surface parallel to the XY plane with vacuum layers (i.e., a slab). This simple user interface enables easy system building for various fcc metals. With these options, a final all-atom model of the (111) gold surface is illustrated in Figure 2B. In this work, experimental densities and surface energies are employed for model validation. Computed densities of 18 fcc metals with different LJ cutoff methods (i.e., 12 cutoff, 10−12 fsw, and LJPME) are in excellent agreement with the experimental data for all supported simulation programs (Table S6 and Figure S1). Solid−vapor interface tensions ($\gamma_{SV}^{(111)}$) for 18 fcc metals with 13 Miller indices were also computed (Figure S2). Figure 2C shows a comparison of the computed and experimental $\gamma_{SV}^{(111)}$ values of 18 fcc metals with three LJ cutoff methods. The 10−12 fsw, 12 cutoff, and LJPME reproduce the surface energy for all fcc metals with less than −6.5, 0.9, and 6.5% deviation, respectively (Tables S4 and S7).

Nanomaterial Modeler provides versatile methods to generate nanoparticle structures and surface modeling. One of the classic models to describe a particle shape is the Wulff construction[65] based on its orientation-dependent surface free energy. The computed surface energies of all fcc metals are presented in Table S4 and are used to generate the Wulff constructions (Figure 2D). One can select any combination of Miller indices and adjust the surface energy values in the user interface. Figure 2D shows the predicted equilibrium shapes using the Wulff construction and the corresponding all-atom models of gold nanoparticles. Selecting (100) and (110) surfaces yields a cuboid (Shape 1). Changing from (110) to (111) produces a truncated octahedron (Shape 2). As the (100) surface energy increases, the (100) surface area decreases, and the shape changes to an octahedron (Shape 3). When a (110) surface is added to Shape 2, the edges are covered with the (110) surface, and the overall nanoparticle shape is closer to a spherical shape (Shape 4).

3.2. Clay Minerals: Kaolinite, Pyrophyllite, Montmorillonite, and Muscovite. Clay minerals have been widely employed not only for industrial applications[66] but also as additive biomaterials for drug delivery.[67] Nanomaterial Modeler provides facile modeling methods for four different clay minerals: kaolinite, pyrophyllite, montmorillonite, and muscovite. Unlike fcc metals, an infinite surface model of clay minerals has image bonds across the PBCs, and 27 image bonds are constructed. In addition, some clay minerals may contain ions between layers, which can be measured by cation exchange capacity (CEC) states. For example, montmorillonite exists in various CEC states with different amounts of Al replaced by Mg. This substitution leaves net negative charges, which attracts cations for charge neutrality. Nanomaterial Modeler provides options for controlling the CEC states by

https://doi.org/10.1021/acs.jctc.1c00996
J. Chem. Theory Comput. 2022, 18, 479−493

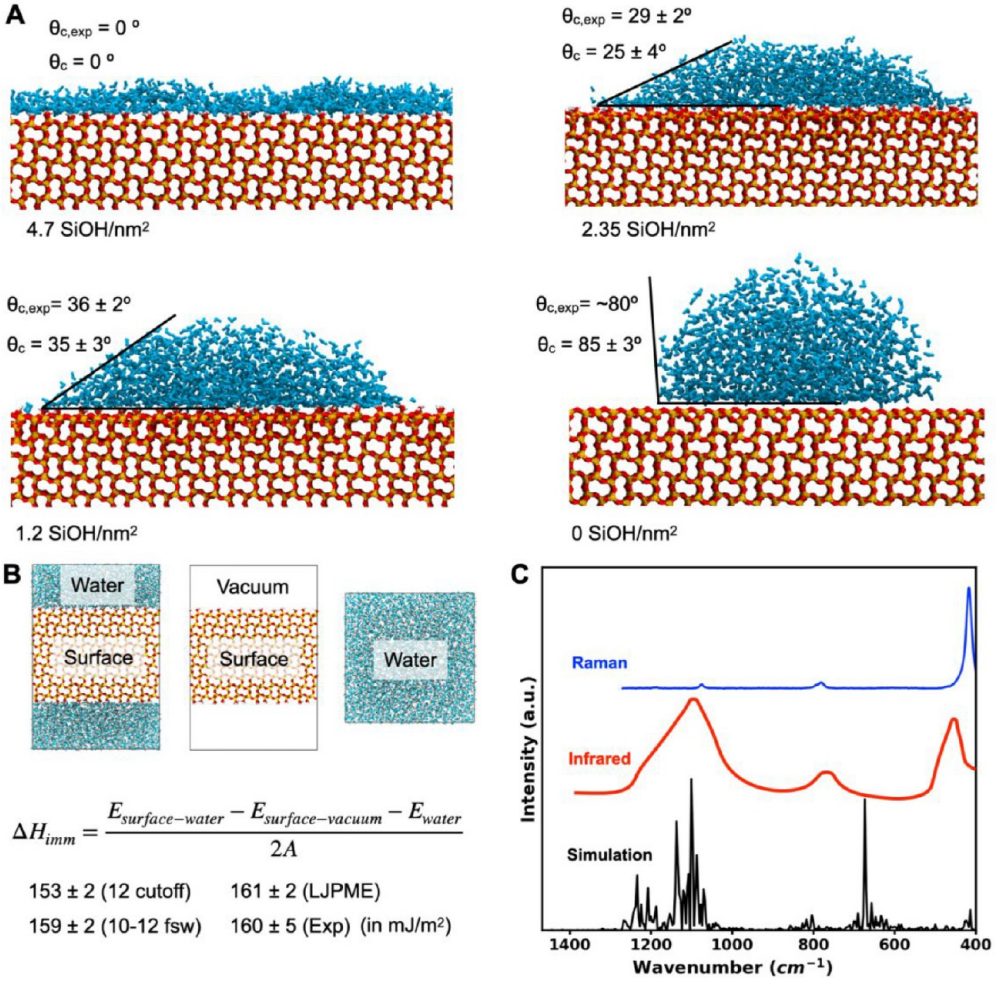

Figure 5. Silica−water interfacial properties and vibrational spectrum. (A) Water contact angles on silica surfaces ranging from Q^3 to Q^4 environments. Experimental results are obtained from ref 75. (B) Heat of immersion of silica surfaces in water. Three systems were generated to compute $E_{surface-water}$, $E_{surface-vacuum}$, and E_{water}, respectively (upper panel). Results of Q^3 surfaces using different LJ cutoff methods and experiments (lower panel) are shown. (C) Vibration spectrum of α-cristobalite from the simulation in comparison with experimental infrared and Raman spectra.

randomly replacing Al with Mg and randomly distributing either Na^+ or K^+.

Figure 3A shows the user interface for building a montmorillonite surface model with 0.333 mmol/100 g CEC, a size of 60 × 60 × 30 Å^3, and *XY* periodicity. Users can select desired CEC states by setting the ratio of the defect (i.e., a ratio of Al and Mg) and ion types. In addition, *X* and *Y* periodic options are selected to build an infinite surface along the *XY* plane. Representative snapshots of three clay minerals (pyrophyllite, montmorillonite, and muscovite) with various CEC states are shown in Figure 3B. The first row displays top views, where layers below the top layer are hidden for clarity. The second row illustrates a side view of each material. Whereas pyrophyllite does not have ions in between layers, montmorillonite and muscovite do, and thus, the number of ions increases as the CEC states become larger. As a result, the spacing between layers of pyrophyllite is ∼2.9 Å, which is smaller than that of the other clay minerals due to the lack of ions between the layers (e.g., ∼3.9 Å for montmorillonite and muscovite). Supported Miller indices and corresponding unit-cell parameters are summarized in Table S5.

The densities, bulk modulus, and Young's modulus of the clay minerals were calculated with three different LJ cutoff methods to validate the model. The computed densities of clay minerals with other LJ cutoff methods show good agreement with the experimental data, with <4% deviation for all supported simulation programs (Table S8 and Figure S3). Figure 3C shows the bulk modulus of muscovite as a function of the applied pressure, which is in good agreement with a previously reported bulk modulus.[68] Also, all of the LJ cutoff methods yield consistent results; 10−12 fsw and LJPME have deviations of −2.6 and 3.7% relative to the 12 cutoff. In experiments, solid−vapor interface tensions (γ_{SV}) show a broad range from 0.050 to 0.200 J/m^2 because the preparation process of the montmorillonite surface with a specific CEC value is difficult, and even if the surface is made, the surface is very sensitive to environmental conditions such as humidity. The computed γ_{SV} of montmorillonite is in a range from 0.087 to 0.113 J/m^2, which is consistent with the range observed in experiments (Table S9). For muscovite, the computed γ_{SV} reproduces the experimental observation with <4% deviation. Note that the energy differences of the computed γ_{SV} among the LJ cutoff methods are negligible for all clay minerals.

Figure 3D represents the Young's modulus of muscovite calculated along the Cartesian directions. The calculated moduli (132.0, 113.4, and 28.6 GPa for the *X*, *Y*, and *Z*

https://doi.org/10.1021/acs.jctc.1c00996
J. Chem. Theory Comput. 2022, 18, 479−493

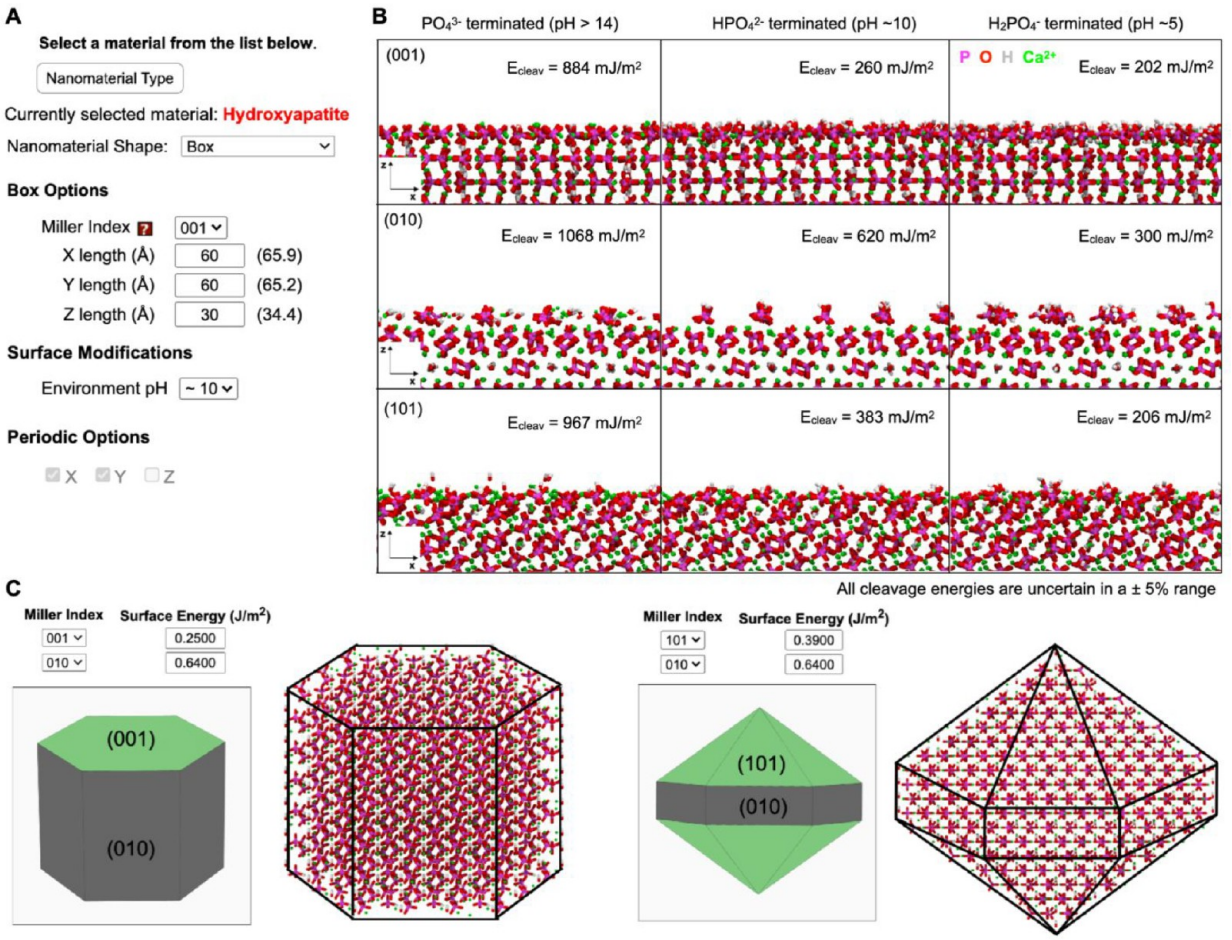

Figure 6. Generation of hydroxyapatite (HAP) surfaces and nanocrystals. (A) User interface for the generation of HAP surfaces. Nanomaterial Modeler supports (001), (010), (020), and (101) surface with three hydrogenation states based on strong basic (pH >14), basic (pH ~10), and mildly acidic (pH ~5) conditions. (B) Illustrative snapshots of relaxed surface models of HAP and calculated cleavage energies in vacuum in different pH environments. (C) Predicted and corresponding all-atom models of rod-like (left) and elongated hexagonal bipyramid (right) shapes of HAP nanocrystals. Phosphate, oxygen, hydrogen, and calcium ion are colored in magenta, red, white, and green, respectively.

directions, respectively) show consistent trends and similar values to previous experimental and DFT results,[69] although the values are ~10% lower. Identical to the reported study, the modulus along the *X* direction is ~16.4% larger than that along the *Y* direction, and the modulus along the *Z* direction is smaller by at least 50% than that along either the *X* or *Y* direction.

3.3. Silica: α-Cristobalite Silica Slab with Different Surface Chemistries. Silicon dioxide and silica are widely available in nature and biologically enriched in various organisms.[70,71] These are also important materials in the semiconductor industry. The simulation of the bulk and surface properties of silica has been of great interest since the emergence of computational modeling methods.[43,72−74] Nanomaterial Modeler provides diverse modeling capabilities of silica that cover various surface chemistries and pH values (i.e., the surface density of silanol and siloxide groups and the degree of ionization) for two shapes (box and sphere).

Figure 4A shows the user interface for building a surface of α-cristobalite with a 4.7 nm^{-2} density of silanol groups. The surface chemistry of silica depends on the surface characteristics (e.g., cleavage plane, particle size, and porosity), heat treatment, and environmental pH.[43] Various forms of silica at high pH contain Q^2 surface environments, which correspond to two silanol groups per superficial silicon atom ($=Si(OH)_2$), and mixed Q^2/Q^3 surface environments, where the Q^3 surface represents one silanol group per silicon atom ($\equiv Si(OH)$). The area density of silanol groups is in a range of 4.7−9.4 nm^{-2} (Figure 4B). Most silica glasses and medium-size nanoparticles (~100 nm) contain 70−90% Q^3 environments on the surface (Figure 4C). The silica surfaces after thermal treatment contain a high portion of Q^4 environments in which siloxide bridges form without silanol groups (Figure 4D). All silanol groups on the silica surface are subject to deprotonation or protonation upon environmental conditions such as the area density of silanol groups, pH, ionic strength of the solution, and type of ions present in solutions. Under the physiological conditions with an ionic strength of 0.1 to 0.3 M of sodium ions, the ionization degree of silanol groups ranges from 0 to 20%. Nanomaterial Modeler supports ionization degrees up to 50% (Figure 4A). Figure 4E−G shows a Q^3 surface with a total Si−O(H,Na) density of 4.7 nm^{-2} with 5, 15, and 25% ionization, respectively.

The silica models show good agreement between the computed and experimental (1) densities, (2) water contact angles on the silica surfaces, (3) heats of immersion of silica surfaces in water, and (4) vibrational properties. Figure 5A shows the water contact angle, θ_c, on charge-neutral silica

https://doi.org/10.1021/acs.jctc.1c00996
J. Chem. Theory Comput. 2022, 18, 479−493

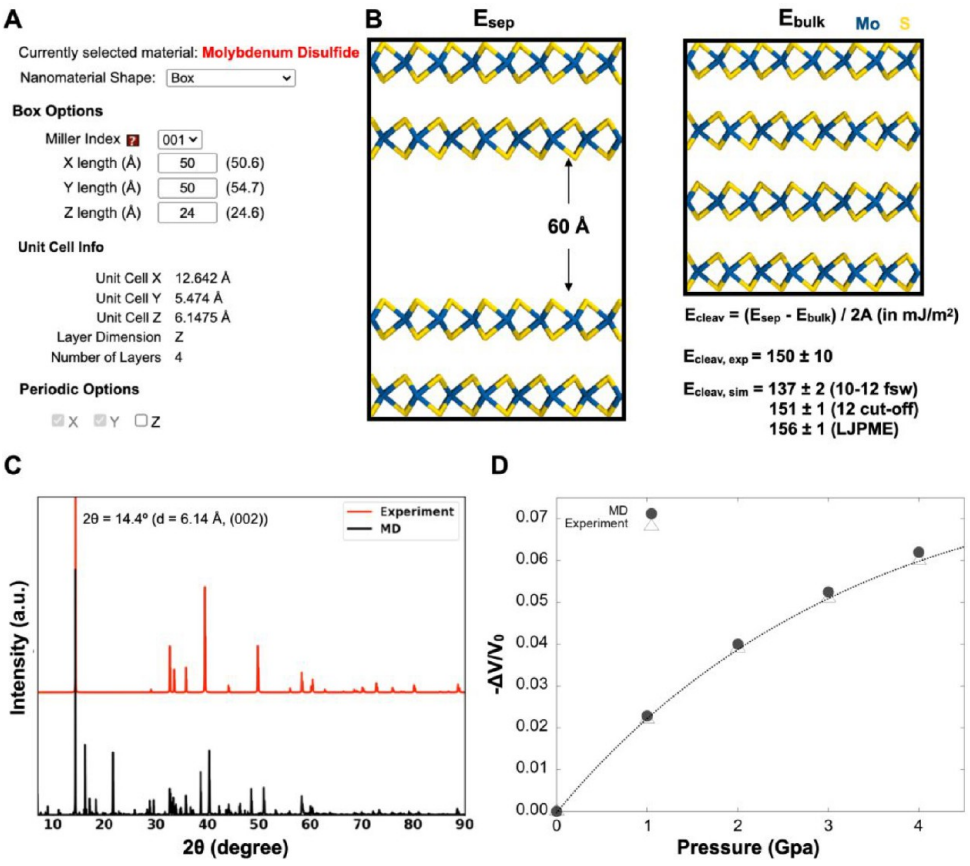

Figure 7. (A) User interface for building 2H-MoS_2 layers. (B) Models used to calculate the cleavage energy comprise a cleaved surface slab of four MoS_2 layers with a 60 Å vacuum layer (left) and the equivalent periodic bulk systems (right). E_{sep} and E_{bulk} represent the potential energies of separated and bulk systems, respectively. A is the surface area. (C) X-ray powder diffraction (XRD) pattern comparison between the experimental data[57] (red) and the MD result (black). (D) Compressibility of bulk MoS_2 from experiment and simulation.

surfaces ranging from Q^3 to Q^4 environments in simulation and experiment.[75] The details of contact-angle calculations are summarized in the Supporting Information and in Figure S4. The Q^3 surface exhibits $\theta_c = 0$. This surface is strongly hydrophilic due to the formation of hydrogen bonds between surface Si−OH groups and water molecules and thus fully wetted with water. Heat treatment from 200 to 1000 °C decreases the area density of surface silanol groups due to the condensation of adjacent silanol groups in Q^2 and Q^3 environments, yielding Q^4 environments. The transition in surface chemistry from Q^3 to Q^4 is modeled with 4.7, 2.35, 1.2, and 0 silanol groups per nm^2. Note that the silanol groups are nonionized to represent interfaces with deionized water. The agreement between simulation and experimental measurements falls within ±3°. The heat of immersion (ΔH_{imm}) represents the enthalpy released upon the immersion of clean particles or surfaces into the water and provides insight into silica−water interactions. Figure 5B shows a computational procedure to compute ΔH_{imm} of Q^3 silica surfaces in water. ΔH_{imm} of Q^3 silica obtained from calorimetric measurements is 160 ± 5 mJ/m^2 at 300 K, and the calculated results show good agreement within the uncertainty for all LJ cutoff methods. The model also reproduces the vibrational frequency of silica with infrared and Raman measurements (Figure 5C and Figure S5). Strong bands at 960−1200 cm^{-1} and 600−800 cm^{-1} correspond to asymmetric and symmetric Si−O−Si stretching vibrations, respectively. The O−Si−O bending vibrations at 400∼500 cm^{-1} and O−H stretching vibrations near 3700 cm^{-1} are also reproduced in the simulation. Although the computed value for one of the bands near 800 cm^{-1} is shifted ∼100 cm^{-1} lower and the intensities of vibrational spectrum are not reproduced due to the lack of a full electronic structure, most peak positions of the vibrational modes are clear and sufficient for monitoring peak shifts in chemically different environments.

3.4. Phosphate Minerals: Hydroxyapatite with Different Surfaces and Wulff Construction. Hydroxyapatite (HAP), $Ca_{10}(PO_4)_6(OH)_2$, is of great importance for human health because it is the major component in human bone and teeth and plays a central role in maladies such as osteoporosis.[44,76] Atomistic models of HAP could facilitate a better understanding of the complex surface chemistry and provide insight into the interaction between biomolecules and HAP. Recent simulation results have shown that specific interactions between HAP surfaces and proteins are strongly dependent on the pH, type of facet, surface defect, and specific details of the amino acid arrangement.[44,77] Surface models of various facets and nanocrystals as a function of pH are introduced in Nanomaterial Modeler to facilitate the research of HAP surface chemistry.

Figure 6A shows the user interface for building a (001) HAP surface with a size of 60 × 60 × 30 $Å^3$ at pH ∼10. Nanomaterial Modeler provides two shapes (box and Wulff construction). The number of possible (hkl) cleavage planes is, in principle, unlimited, but cleavage preferably occurs in (hkl) directions with weaker nonbonded interactions. Nanomaterial

https://doi.org/10.1021/acs.jctc.1c00996
J. Chem. Theory Comput. 2022, 18, 479−493

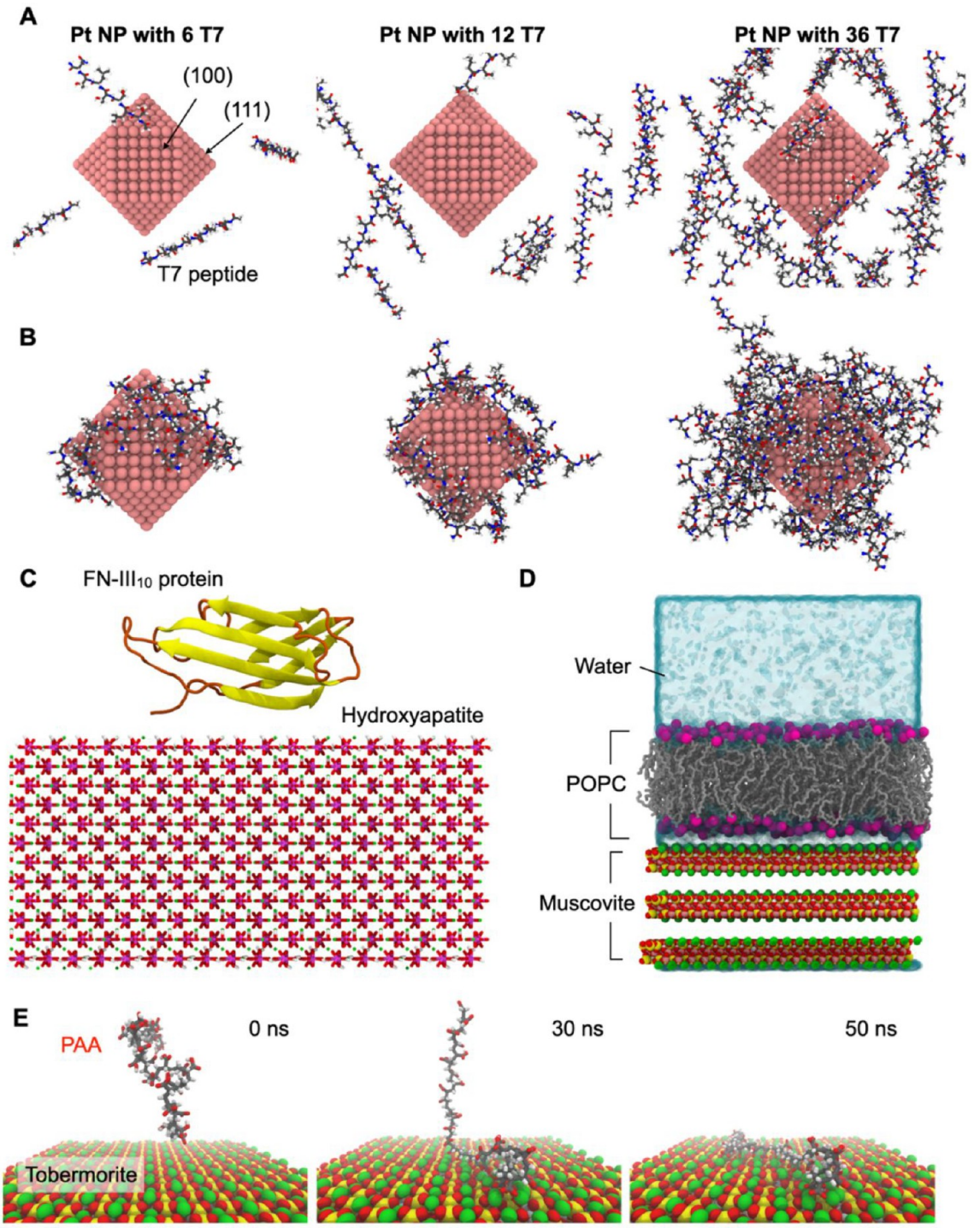

Figure 8. Illustrative snapshots of (A) initial and (B) final simulation systems for a platinum (Pt) nanoparticle with T7 peptides. Platinum, nitrogen, carbon, oxygen, and hydrogen atoms are colored in pink, blue, gray, red, and white, respectively. (C) Hydroxyapatite surface with FN-III10 protein. Hydroxyapatite is colored as in Figure 4. FN-III10 proteins are represented in a cartoon with different colors based on the secondary structures (yellow for β-sheet and orange for coil and turn). (D) Supported lipid bilayer composed of 1-palmitoyl-2-oleoyl-*sn*-phophatidylcholine (POPC) and muscovite. Phosphorus, carbon, silica, oxygen, hydrogen, calcium, and aluminum atoms are colored in magenta, gray, yellow, red, white, green, and pink, respectively. (E) Snapshots of poly(acrylic acid) adsorption on a tobermorite (004) facet. The color code is the same as in panel D. Water molecules are omitted for clarity, except for in panel D.

Modeler offers the common cleavage planes of HAP, (001), (010), (020), and (101), and surface models of HAP under various pH conditions, including pH ∼5, ∼10, and >14. (See the details in the Supporting Information.) MD simulations were performed to investigate the cleavage energies of the common low index planes of HAP (Figure 6B). The computed cleavage energies of PO_4^{3-}-terminated surfaces range from 897.0 to 1223.3 mJ/m^2 and increase in the following order: (001) < (101) < (010) < (020). Note that the cleavage energy differences among the simulation packages are negligible (Table S9). For the LJ cutoff methods, 10−12 fsw and LJPME produce only −2.4 and 3.2% deviations relative to the 12 cutoff

https://doi.org/10.1021/acs.jctc.1c00996
J. Chem. Theory Comput. 2022, 18, 479−493

method (Table S10). Such a small difference compared with the deviations observed for fcc metals arises from the fact that electrostatic interactions dominate the HAP surface energy. (See the details in the Supporting Information.) In an experiment, the preparation of ideal cleaved surfaces of HAP is complex because they are hygroscopic and thus sensitive to environmental conditions such as humidity. To our knowledge, direct measurements of cleavage energies in vacuum have not been reported. Nevertheless, the cleavage energies of minerals with similar chemical compositions and previously calculated cleavage energies for HAP are in good agreement with the current simulation results. (See Table S10.)

Nanomaterial Modeler enables modeling of HAP nanocrystals (i.e., Wulff construction) and various surface models. Figure 6C illustrates the predicted shapes of the HAP nanocrystal and final all-atom models according to the combination of Miller indices and corresponding surface energies. Like the Wulff construction of gold nanoparticles in Figure 2, one can freely change the surface energy values in the text box and add/delete surfaces by clicking the ± button. In addition, the environment pH option can be specified during Wulff construction. Because cleavage energies are highly affected by environment pH, Nanomaterial Modeler automatically updates energy values and predicts corresponding shapes based on the selected pH range.

3.5. Transition Metal Dichalcogenide: MoS_2. Two-dimensional (2D) materials, including graphene and TMDCs, such as molybdenum disulfide (MoS_2), have received significant attention due to their unique structural and electronic properties.[78,79] Nanomaterial Modeler provides a facile modeling capability for graphene and 2H-MoS_2.

Figure 7A shows the user interface for building four 2H-MoS_2 layers with a size of 50 × 50 × 24 Å^3. In the Unit Cell Info section, one can set the number of MoS_2 layers to be generated according to the *Z*-length value in the Box Options. Note that MoS_2 is limited to XY-PBC, as there is no information available for surface-end modification. The cleavage energy of the basal plane of a layered material is a key property for its applications. A potential energy difference of two systems (i.e., a box of surface slabs separated by a 60 Å vacuum layer (E_{sep}) and an equivalent periodic bulk model without a vacuum layer (E_{bulk})) was computed with 10−12 fsw, 12 cutoff, and LJPME using four simulation packages to evaluate the cleavage energy of MoS_2 (Figure 7B and Supporting Information). The results agree with an experimental observation of 150 ± 10 mJ/m^2 for 12 cutoff. The use of different cutoff methods yields 137 ± 2 mJ/m^2 (10−12 fsw) and 156 ± 1 mJ/m^2 (LJPME), respectively. These relatively high deviations are also observed in the fcc metal cases, as LJ interactions are the major component for their cleavage energy. For MoS_2, the contributions of LJ and electrostatic interactions to the cleavage energy are 93 and 7%, respectively. This indicates that when the LJ interaction is the main contributing factor to the cleavage energy, the LJ parameter adjustments for 10−12 fsw and LJPME methods are required to achieve the level of accuracy at experiment.

The structural and mechanical properties as well as the surface properties are essential factors for validating the MoS_2 model.[15] Figure 7C shows the computed XRD pattern from experiment and simulation. The characteristic peak of MoS_2 is observed at 14.4°, corresponding to the (002) plane, and agrees well with the experimental observation. For mechanical properties, the compressibility was computed with the 12 cutoff method by recording the volume change at different pressures (1, 2, 3, and 4 GPa) and compared with the experiment (Figure 7D). The simulation results are identical to the experiment up to ∼2 GPa. Even when the pressure exceeds 2 GPa, the difference between the computed and experimental data remains below a 2% deviation.

3.6. Complex System. Several complex nanobio systems were modeled and simulated to illustrate the potential use of Nanomaterial Modeler in combination with other CHARMM-GUI modules. Note that these illustrative systems are chosen to show the new capability of Nanomaterial Modeler but not for the FF validation. As a first example, a platinum (Pt) nanoparticle system with T7 peptides (acyl-TLTTLTN-amide) was built using three modules in CHARMM-GUI: Nanomaterial Modeler for the Pt nanoparticle, PDB Reader & Manipulator[7,80] for T7 peptides, and Multicomponent Assembler for the assembly of all models and solvation (Figure 8A). A cuboctahedron Pt nanoparticle was generated using Wulff construction (Shape 2 in Figure 2 and Figure S6) and located at the system center. T7 peptides were randomly distributed in the system with 3, 6, 12, 18, and 36 peptides corresponding to concentrations of 5, 10, 20, 50, and 100 μg/mL. (See the Methods and the Supporting Information for details of the system building and simulation methods.) After MD simulations of 200 ns duration, all T7 peptides were adsorbed onto the nanoparticle surface at all concentration levels (Figure 8B). At low concentration (<20 μg/mL), the binding of the T7 peptides to the Pt nanoparticle preferentially occurs near edges as opposed to the inner portions of the (100) facets. This is due to the substantially reduced binding of water at the edges, which is consistent with previously reported data.[81] These simulations provide insight into the mechanisms of nanocrystal growth and the spatial distribution of facet-specific ligands as a function of concentration.

As a second example, 10 type-III modules of fibronectin (FN-III$_{10}$, PDB ID: 1TTF[82]) on a HAP surface were generated (Figure 8C). Fibronectin (FN) is known to regulate the cell adhesion, growth, differentiation, or survival of osteoblasts and to support osteogenic cell responses in vitro.[83] This complex nanobio interface system can be readily generated using a combination of Nanomaterial Modeler, PDB Reader, and Multicomponent Assembler modules. This system can be used to investigate the effects of the HAP surface properties on the adsorption of FN modules, which is important because the surface topology may modulate the biological activity of FN and the corresponding cell adhesion process.

The third example consists of a supported lipid bilayer (SLB), which is a popular model of cell membranes with potential biotechnological applications.[84] Many experimental techniques such as atomic force microscopy (AFM), quartz crystal microbalance with dissipation monitoring (QCM-D), and ellipsometry have been employed to investigate the structure and physical properties of lipid bilayers reconstituted with membrane proteins;[85,86] however, most of these methods provide only superficial information or lack molecular-level insight into underlying mechanisms. Figure 8D shows an SLB system built using a combination of Nanomaterial Modeler, Membrane Builder,[87−89] and Multicomponent Assembler modules. (See the Methods and the Supporting Information.)

In addition to various nanobio interfaces, Nanomaterial Modeler can also be used to build polymer-containing nanomaterial systems (i.e., nanopolymers interfaces). As a final example, a nanopolymer complex system that consists of a

https://doi.org/10.1021/acs.jctc.1c00996
J. Chem. Theory Comput. 2022, 18, 479−493

cement mineral (in this case, tobermorite) and poly(acrylic acid) (PAA) was investigated. It is known that PAA strongly binds to the cement surface via ionic or possibly chelate binding and induces the cement to harden. Three modules in CHARMM-GUI were employed: Nanomaterial Modeler for tobermorite, Polymer Builder[60] for PAA, and Multicomponent Assembler for integration and solvation. A tobermorite (004) slab was located in the simulation box, and a 60% ionized PAA chain was placed 10 Å above the surface (Figure 8E). In an early simulation stage, carboxylates in the PAA side chains began to interact with the surface via strong ionic bonds with Ca^{2+} ions; finally, the entire polymer chain was adsorbed on the surface.

4. CONCLUSIONS

This work presents Nanomaterial Modeler in CHARMM-GUI, a web-based cyberinfrastructure for building all-atom models of various nanomaterials and providing all necessary FF and configurational files for MD simulations. The model-building workflow is generalized and automated in two steps: (i) building a bulk crystal through the duplication and translation of a unit-cell structure and (ii) applying image patches and capping unbalanced atoms based on the periodicity and chemical environment. Nanomaterial Modeler's versatile and efficient modeling features are illustrated by building various nanomaterial surface models and equilibrium nanoparticle shapes. Moreover, the transferability of nanomaterial models among the simulation programs is assessed by single-point energy calculations, which yield 0.01% relative absolute energy differences for various surface models and equilibrium nanoparticle shapes. The significance of this work is that Nanomaterial Modeler provides a convenient modeling capability for various nanomaterial systems. Generated nanomaterial models can be used to model complex systems with other CHARMM-GUI modules, as demonstrated here with selected representative test cases.

To assess the transferability of our models and the IFF, we have investigated the effect of LJ cutoff methods on the structural, mechanical, and thermodynamic properties of nanomaterials. We have determined that the different LJ cutoff methods exhibit overall consistent results for most nanomaterial cases. The exceptions are nanomaterials for which LJ interactions are a major component for their cleavage energy. Such systems exhibit relatively larger deviations (up to 8%) compared with the electrostatic-driven materials if an LJ cutoff other than 12 Å is used. However, in most cases, deviations are minor, and consistent cutoffs or adjustments in the ϵ and σ parameters can be explored. Future work will include testing transferability for other nanomaterial properties and comparison with reactive and machine-learning FFs through the OpenKIM framework.[90] We hope that Nanomaterial Modeler can be useful for carrying out innovative and novel nanomaterial modeling and simulation research to acquire insight into the structures, dynamics, and underlying mechanisms of complex nanobio and nanopolymer interface systems.

■ ASSOCIATED CONTENT

Supporting Information

The Supporting Information is available free of charge at https://pubs.acs.org/doi/10.1021/acs.jctc.1c00996.

Computational Details S1−S7: Detailed methods for simulation protocols of various simulation packages, nanomaterial model preparations, measurement of structural, mechanical, vibrational, and thermodynamic properties, and preparations of complex nanobio and nanopolymer systems. Table S1: Simulation parameters for the nanomaterial simulations. Table S2: Isothermal compressibility of nanomaterials. Table S3: Single-point energy calculations of various simulation programs. Tables S4 and S5: Lattice parameters of supported nanomaterials. Table S6: Computed densities of 18 fcc metals with three LJ cutoff methods. Figure S1: Error estimation of computed densities of fcc metals with different LJ cutoff methods. Figure S2: Illustration of the solid−vapor surface energy calculation. Table S7: Effect of LJ cutoff methods on the solid−vapor surface energy of fcc metals. Table S8 and Figure S3: Computed densities of nanomaterials with three LJ cutoff methods. Figure S4: Illustration of contact-angle measurements of the silica surface. Figure S5: Velocity autocorrelation function of α-cristobalite. Table S9: computed surface energies of nanomaterials with three LJ cutoff methods. Table S10: Computed cleavage energies of hydroxyapatite under various pH conditions. Figure S6: illustration of Wulff construction of platinum (PDF)

■ AUTHOR INFORMATION

Corresponding Author

Wonpil Im − *Departments of Biological Sciences, Chemistry, Bioengineering, and Computer Science and Engineering, Lehigh University, Bethlehem, Pennsylvania 18015, United States;* orcid.org/0000-0001-5642-6041; Email: wonpil@lehigh.edu

Authors

Yeol Kyo Choi − *Department of Biological Sciences, Lehigh University, Bethlehem, Pennsylvania 18015, United States;* orcid.org/0000-0002-4218-7139

Nathan R. Kern − *Department of Computer Science, Lehigh University, Bethlehem, Pennsylvania 18015, United States;* orcid.org/0000-0003-0936-7274

Seonghan Kim − *Department of Bioengineering, Lehigh University, Bethlehem, Pennsylvania 18015, United States;* orcid.org/0000-0002-1890-0061

Krishan Kanhaiya − *Department of Chemical and Biological Engineering, University of Colorado at Boulder, Boulder, Colorado 80301, United States;* orcid.org/0000-0002-3622-2655

Yaser Afshar − *Department of Aerospace Engineering and Mechanics, University of Minnesota, Minneapolis, Minnesota 55455, United States*

Sun Hee Jeon − *Department of Biological Sciences, Lehigh University, Bethlehem, Pennsylvania 18015, United States*

Sunhwan Jo − *Leadership Computing Facility, Argonne National Laboratory, Argonne, Illinois 60439, United States*

Bernard R. Brooks − *Laboratory of Computational Biology, National Heart, Lung and Blood Institute, National Institutes of Health, Bethesda, Maryland 20892, United States;* orcid.org/0000-0002-3586-2730

Jumin Lee − *Department of Biological Sciences, Lehigh University, Bethlehem, Pennsylvania 18015, United States;* orcid.org/0000-0002-1008-0118

Ellad B. Tadmor − *Department of Aerospace Engineering and Mechanics, University of Minnesota, Minneapolis, Minnesota 55455, United States;* orcid.org/0000-0003-3311-6299

https://doi.org/10.1021/acs.jctc.1c00996
J. Chem. Theory Comput. 2022, 18, 479−493

Hendrik Heinz − *Department of Chemical and Biological Engineering, University of Colorado at Boulder, Boulder, Colorado 80301, United States;* orcid.org/0000-0002-6776-7404

Complete contact information is available at: https://pubs.acs.org/10.1021/acs.jctc.1c00996

Author Contributions

#Y.K.C., N.R.K., and S.K. contributed equally to this work.

Notes

The authors declare no competing financial interest.

Nanomaterial Modeler can be accessed through the following link: https://www.charmm-gui.org/input/nanomaterial. Under "References for Nanomaterial Modeler": On the front page of Nanomaterial Modeler, one can also obtain initial coordinates, topology, and configuration files of five representative systems, which include (1) surface tension of Au {111} surface, (2) surface energy of muscovite, (3) contact-angle measurement of silica surfaces, (4) Pt nanoparticle with T7 peptides, and (5) supported lipid bilayer system. Detailed procedures on how to build nanomaterial models using Nanomaterial Modeler are described in a video demonstration (https://www.charmm-gui.org/demo/nanomaterial). Tutorial 1: Overview of Nanomaterial Modeler; Tutorial 2: Surface model and Wulff construction of fcc metal; Tutorial 3: Building clay mineral models; Tutorial 4: Building calcium sulfate models; Tutorial 5: Building cement mineral models; Tutorial 6: Modeling nanoparticle and surfaces of silica; Tutorial 7: Modeling nanocrystal and surfaces of hydroxyapatite; Tutorial 8: Modeling molybdenum disulfide; Tutorial 9: Modeling carbon nanotube and graphene. Questions related to the performance of the IFF for the nanomaterials and related simulation settings can be directed to H.H. (hendrik.heinz@colorado.edu).

■ ACKNOWLEDGMENTS

This work was partially supported by grants from NIH GM138472 (W.I.), NSF OAC-1931343 (W.I.), NSF OAC-1931587 (H.H.), and NSF OAC-1931304 (E.B.T.).

■ REFERENCES

(1) Yang, Y.; Chen, C. C.; Scott, M. C.; Ophus, C.; Xu, R.; Pryor, A.; Wu, L.; Sun, F.; Theis, W.; Zhou, J.; Eisenbach, M.; Kent, P. R.; Sabirianov, R. F.; Zeng, H.; Ercius, P.; Miao, J. Deciphering chemical order/disorder and material properties at the single-atom level. *Nature* **2017**, *542*, 75−79.

(2) Yeom, B.; Sain, T.; Lacevic, N.; Bukharina, D.; Cha, S. H.; Waas, A. M.; Arruda, E. M.; Kotov, N. A. Abiotic tooth enamel. *Nature* **2017**, *543*, 95−98.

(3) Chen, J.; Zhu, E.; Liu, J.; Zhang, S.; Lin, Z.; Duan, X.; Heinz, H.; Huang, Y.; De Yoreo, J. J. Building two-dimensional materials one row at a time: Avoiding the nucleation barrier. *Science* **2018**, *362*, 1135−1139.

(4) Heinz, H.; Pramanik, C.; Heinz, O.; Ding, Y.; Mishra, R. K.; Marchon, D.; Flatt, R. J.; Estrela-Lopis, I.; Llop, J.; Moya, S.; Ziolo, R. F. Nanoparticle decoration with surfactants: Molecular interactions, assembly, and applications. *Surf. Sci. Rep.* **2017**, *72*, 1−58.

(5) Bai, Y.; Zhang, R.; Ye, X.; Zhu, Z.; Xie, H.; Shen, B.; Cai, D.; Liu, B.; Zhang, C.; Jia, Z.; Zhang, S.; Li, X.; Wei, F. Carbon nanotube bundles with tensile strength over 80 GPa. *Nat. Nanotechnol.* **2018**, *13*, 589−595.

(6) Lee, J.; Cheng, X.; Swails, J. M.; Yeom, M. S.; Eastman, P. K.; Lemkul, J. A.; Wei, S.; Buckner, J.; Jeong, J. C.; Qi, Y.; Jo, S.; Pande, V. S.; Case, D. A.; Brooks, C. L., 3rd; MacKerell, A. D., Jr.; Klauda, J. B.; Im, W. CHARMM-GUI Input Generator for NAMD, GROMACS, AMBER, OpenMM, and CHARMM/OpenMM Simulations Using the CHARMM36 Additive Force Field. *J. Chem. Theory Comput.* **2016**, *12*, 405−13.

(7) Jo, S.; Kim, T.; Iyer, V. G.; Im, W. CHARMM-GUI: a web-based graphical user interface for CHARMM. *J. Comput. Chem.* **2008**, *29*, 1859−65.

(8) Heinz, H.; Lin, T.-J.; Kishore Mishra, R.; Emami, F. S. Thermodynamically consistent force fields for the assembly of inorganic, organic, and biological nanostructures: the INTERFACE force field. *Langmuir* **2013**, *29*, 1754−1765.

(9) Huang, J.; MacKerell, A. D., Jr CHARMM36 all-atom additive protein force field: validation based on comparison to NMR data. *J. Comput. Chem.* **2013**, *34*, 2135−45.

(10) Wang, J.; Wolf, R. M.; Caldwell, J. W.; Kollman, P. A.; Case, D. A. Development and testing of a general amber force field. *J. Comput. Chem.* **2004**, *25*, 1157−74.

(11) Heinz, H.; Lin, T.-J.; Kishore Mishra, R.; Emami, F. S. Thermodynamically consistent force fields for the assembly of inorganic, organic, and biological nanostructures: the INTERFACE force field. *Langmuir* **2013**, *29*, 1754−65.

(12) Heinz, H.; Ramezani-Dakhel, H. Simulations of inorganic-bioorganic interfaces to discover new materials: insights, comparisons to experiment, challenges, and opportunities. *Chem. Soc. Rev.* **2016**, *45*, 412−48.

(13) Mishra, R. K.; Kanhaiya, K.; Winetrout, J. J.; Flatt, R. J.; Heinz, H. Force field for calcium sulfate minerals to predict structural, hydration, and interfacial properties. *Cem. Concr. Res.* **2021**, *139*, 106262.

(14) Mark, L. O.; Zhu, C.; Medlin, J. W.; Heinz, H. Understanding the Surface Reactivity of Ligand-Protected Metal Nanoparticles for Biomass Upgrading. *ACS Catal.* **2020**, *10*, 5462−5474.

(15) Liu, J.; Zeng, J.; Zhu, C.; Miao, J.; Huang, Y.; Heinz, H. Interpretable molecular models for molybdenum disulfide and insight into selective peptide recognition. *Chem. Sci.* **2020**, *11*, 8708−8722.

(16) Schappals, M.; Mecklenfeld, A.; Kröger, L.; Botan, V.; Köster, A.; Stephan, S.; García, E. J.; Rutkai, G.; Raabe, G.; Klein, P.; et al. Round robin study: Molecular simulation of thermodynamic properties from models with internal degrees of freedom. *J. Chem. Theory Comput.* **2017**, *13*, 4270−4280.

(17) Franco-Ulloa, S.; Riccardi, L.; Rimembrana, F.; Pini, M.; De Vivo, M. NanoModeler: A Webserver for Molecular Simulations and Engineering of Nanoparticles. *J. Chem. Theory Comput.* **2019**, *15*, 2022−2032.

(18) Yan, X.; Sedykh, A.; Wang, W.; Yan, B.; Zhu, H. Construction of a web-based nanomaterial database by big data curation and modeling friendly nanostructure annotations. *Nat. Commun.* **2020**, *11*, 2519.

(19) Hjorth Larsen, A.; Jorgen Mortensen, J.; Blomqvist, J.; Castelli, I. E.; Christensen, R.; Dułak, M.; Friis, J.; Groves, M. N.; Hammer, B.; Hargus, C.; et al. The atomic simulation environment—a Python library for working with atoms. *J. Phys.: Condens. Matter* **2017**, *29*, 273002.

(20) Fortunato, M. E.; Colina, C. M. pysimm: A python package for simulation of molecular systems. *SoftwareX* **2017**, *6*, 7−12.

(21) Summers, A. Z.; Gilmer, J. B.; Iacovella, C. R.; Cummings, P. T.; McCabe, C. MoSDeF, a python framework enabling large-scale computational screening of soft matter: Application to chemistry-property relationships in lubricating monolayer films. *J. Chem. Theory Comput.* **2020**, *16*, 1779−1793.

(22) Nikoulis, G.; Grammatikopoulos, P.; Steinhauer, S.; Kioseoglou, J. NanoMaterialsCAD: Flexible Software for the Design of Nanostructures. *Adv. Theory Simul.* **2021**, *4*, 2000232.

(23) BIOVIA, Dassault Systèmes. *Material Studio*; Dassault Systèmes: San Diego, 2020.

(24) *Schrödinger Release 2021-2: Maestro*; Schrödinger, LLC: New York, 2021.

(25) te Velde, G.; Bickelhaupt, F. M.; Baerends, E. J.; Fonseca Guerra, C.; van Gisbergen, S. J. A.; Snijders, J. G.; Ziegler, T. Chemistry with ADF. *J. Comput. Chem.* **2001**, *22*, 931−967.

(26) Brooks, B. R.; Brooks, C. L., 3rd; Mackerell, A. D., Jr.; Nilsson, L.; Petrella, R. J.; Roux, B.; Won, Y.; Archontis, G.; Bartels, C.; Boresch, S.; Caflisch, A.; Caves, L.; Cui, Q.; Dinner, A. R.; Feig, M.; Fischer, S.; Gao, J.; Hodoscek, M.; Im, W.; Kuczera, K.; Lazaridis, T.; Ma, J.; Ovchinnikov, V.; Paci, E.; Pastor, R. W.; Post, C. B.; Pu, J. Z.; Schaefer, M.; Tidor, B.; Venable, R. M.; Woodcock, H. L.; Wu, X.; Yang, W.; York, D. M.; Karplus, M. CHARMM: the biomolecular simulation program. *J. Comput. Chem.* **2009**, *30*, 1545−614.
(27) Phillips, J. C.; Braun, R.; Wang, W.; Gumbart, J.; Tajkhorshid, E.; Villa, E.; Chipot, C.; Skeel, R. D.; Kale, L.; Schulten, K. Scalable molecular dynamics with NAMD. *J. Comput. Chem.* **2005**, *26*, 1781−802.
(28) Abraham, M. J.; Murtola, T.; Schulz, R.; Páll, S.; Smith, J. C.; Hess, B.; Lindahl, E. GROMACS: High performance molecular simulations through multi-level parallelism from laptops to supercomputers. *SoftwareX* **2015**, *1−2*, 19−25.
(29) Case, D. A.; Cheatham, T. E., 3rd; Darden, T.; Gohlke, H.; Luo, R.; Merz, K. M., Jr.; Onufriev, A.; Simmerling, C.; Wang, B.; Woods, R. J. The Amber biomolecular simulation programs. *J. Comput. Chem.* **2005**, *26*, 1668−88.
(30) Jung, J.; Mori, T.; Kobayashi, C.; Matsunaga, Y.; Yoda, T.; Feig, M.; Sugita, Y. GENESIS: a hybrid-parallel and multi-scale molecular dynamics simulator with enhanced sampling algorithms for biomolecular and cellular simulations. *Wiley Interdiscip. Rev.: Comput. Mol. Sci.* **2015**, *5*, 310−323.
(31) Plimpton, S. Fast parallel algorithms for short-range molecular dynamics. *J. Comput. Phys.* **1995**, *117*, 1−19.
(32) Rackers, J. A.; Wang, Z.; Lu, C.; Laury, M. L.; Lagardere, L.; Schnieders, M. J.; Piquemal, J. P.; Ren, P.; Ponder, J. W. Tinker 8: Software Tools for Molecular Design. *J. Chem. Theory Comput.* **2018**, *14*, 5273−5289.
(33) Bowers, K. J.; Chow, D. E.; Xu, H.; Dror, R. O.; Eastwood, M. P.; Gregersen, B. A.; Klepeis, J. L.; Kolossvary, I.; Moraes, M. A.; Sacerdoti, F. D. In *Scalable Algorithms for Molecular Dynamics Simulations on Commodity Clusters*; SC'06: Proceedings of the 2006 ACM/IEEE Conference on Supercomputing; IEEE: 2006; pp 43−43.
(34) Eastman, P.; Swails, J.; Chodera, J. D.; McGibbon, R. T.; Zhao, Y.; Beauchamp, K. A.; Wang, L. P.; Simmonett, A. C.; Harrigan, M. P.; Stern, C. D.; Wiewiora, R. P.; Brooks, B. R.; Pande, V. S. OpenMM 7: Rapid development of high performance algorithms for molecular dynamics. *PLoS Comput. Biol.* **2017**, *13*, e1005659.
(35) Klauda, J. B.; Venable, R. M.; Freites, J. A.; O'Connor, J. W.; Tobias, D. J.; Mondragon-Ramirez, C.; Vorobyov, I.; MacKerell, A. D., Jr.; Pastor, R. W. Update of the CHARMM all-atom additive force field for lipids: validation on six lipid types. *J. Phys. Chem. B* **2010**, *114*, 7830−43.
(36) Huang, J.; Rauscher, S.; Nawrocki, G.; Ran, T.; Feig, M.; de Groot, B. L.; Grubmuller, H.; MacKerell, A. D., Jr. CHARMM36m: an improved force field for folded and intrinsically disordered proteins. *Nat. Methods* **2017**, *14*, 71−73.
(37) *Interface Force Field (IFF) and a Surface Model Database.* https://bionanostructures.com/interface-md/, 2013−2021.
(38) Heinz, H.; Vaia, R. A.; Farmer, B. L.; Naik, R. R. Accurate Simulation of Surfaces and Interfaces of Face-Centered Cubic Metals Using 12−6 and 9−6 Lennard-Jones Potentials. *J. Phys. Chem. C* **2008**, *112*, 17281−17290.
(39) Kanhaiya, K.; Kim, S.; Im, W.; Heinz, H. Accurate simulation of surfaces and interfaces of ten FCC metals and steel using Lennard−Jones potentials. *npj Comput. Mater.* **2021**, *7*, No. 17.
(40) Heinz, H. Clay minerals for nanocomposites and biotechnology: surface modification, dynamics and responses to stimuli. *Clay Miner.* **2012**, *47*, 205−230.
(41) Mishra, R. K.; Flatt, R. J.; Heinz, H. Force Field for Tricalcium Silicate and Insight into Nanoscale Properties: Cleavage, Initial Hydration, and Adsorption of Organic Molecules. *J. Phys. Chem. C* **2013**, *117*, 10417−10432.
(42) Mishra, R. K.; Fernandez-Carrasco, L.; Flatt, R. J.; Heinz, H. A force field for tricalcium aluminate to characterize surface properties, initial hydration, and organically modified interfaces in atomic resolution. *Dalton Trans.* **2014**, *43*, 10602−16.
(43) Emami, F. S.; Puddu, V.; Berry, R. J.; Varshney, V.; Patwardhan, S. V.; Perry, C. C.; Heinz, H. Force Field and a Surface Model Database for Silica to Simulate Interfacial Properties in Atomic Resolution. *Chem. Mater.* **2014**, *26*, 2647−2658.
(44) Lin, T.-J.; Heinz, H. Accurate Force Field Parameters and pH Resolved Surface Models for Hydroxyapatite to Understand Structure, Mechanics, Hydration, and Biological Interfaces. *J. Phys. Chem. C* **2016**, *120*, 4975−4992.
(45) Pramanik, C.; Gissinger, J. R.; Kumar, S.; Heinz, H. Carbon Nanotube Dispersion in Solvents and Polymer Solutions: Mechanisms, Assembly, and Preferences. *ACS Nano* **2017**, *11*, 12805−12816.
(46) Wang, J.; Wolf, R. M.; Caldwell, J. W.; Kollman, P. A.; Case, D. A. Development and testing of a general amber force field. *J. Comput. Chem.* **2004**, *25*, 1157−1174.
(47) Best, R. B.; Zhu, X.; Shim, J.; Lopes, P. E.; Mittal, J.; Feig, M.; MacKerell, A. D., Jr Optimization of the additive CHARMM all-atom protein force field targeting improved sampling of the backbone ϕ, ψ and side-chain χ1 and χ2 dihedral angles. *J. Chem. Theory Comput.* **2012**, *8*, 3257−3273.
(48) Klauda, J. B.; Venable, R. M.; Freites, J. A.; O'Connor, J. W.; Tobias, D. J.; Mondragon-Ramirez, C.; Vorobyov, I.; MacKerell, A. D., Jr; Pastor, R. W. Update of the CHARMM all-atom additive force field for lipids: validation on six lipid types. *J. Phys. Chem. B* **2010**, *114*, 7830−7843.
(49) Hart, K.; Foloppe, N.; Baker, C. M.; Denning, E. J.; Nilsson, L.; MacKerell, A. D., Jr Optimization of the CHARMM additive force field for DNA: Improved treatment of the BI/BII conformational equilibrium. *J. Chem. Theory Comput.* **2012**, *8*, 348−362.
(50) Schmid, N.; Eichenberger, A. P.; Choutko, A.; Riniker, S.; Winger, M.; Mark, A. E.; van Gunsteren, W. F. Definition and testing of the GROMOS force-field versions 54A7 and 54B7. *Eur. Biophys. J.* **2011**, *40*, 843−856.
(51) Kaminski, G. A.; Friesner, R. A.; Tirado-Rives, J.; Jorgensen, W. L. Evaluation and reparametrization of the OPLS-AA force field for proteins via comparison with accurate quantum chemical calculations on peptides. *J. Phys. Chem. B* **2001**, *105*, 6474−6487.
(52) Hirschfelder, J. O.; Curtiss, C. F.; Bird, R. B. Molecular Theory of Gases and Liquids. In *Molecular Theory of Gases and Liquids*; Wiley: New York, 1964.
(53) Heinz, H.; Castelijns, H. J.; Suter, U. W. Structure and phase transitions of alkyl chains on mica. *J. Am. Chem. Soc.* **2003**, *125*, 9500−9510.
(54) Steinbach, P. J.; Brooks, B. R. New spherical-cutoff methods for long-range forces in macromolecular simulation. *J. Comput. Chem.* **1994**, *15*, 667−683.
(55) Shirts, M. R.; Klein, C.; Swails, J. M.; Yin, J.; Gilson, M. K.; Mobley, D. L.; Case, D. A.; Zhong, E. D. Lessons learned from comparing molecular dynamics engines on the SAMPL5 dataset. *J. Comput.-Aided Mol. Des.* **2017**, *31*, 147−161.
(56) Lide, D. R. *CRC Handbook of Chemistry and Physics*, 84th ed.; CRC Press: Boca Raton, FL, 2004; Vol. *85*.
(57) Schönfeld, B.; Huang, J. J.; Moss, S. C. Anisotropic mean-square displacements (MSD) in single-crystals of 2H- and 3R-MoS2. *Acta Crystallogr., Sect. B: Struct. Sci.* **1983**, *39*, 404−407.
(58) Heaney, P. J.; Prewitt, C. T.; Gibbs, G. V. *Silica: Physical Behavior, Geochemistry, and Materials Applications*; Walter de Gruyter GmbH & Co KG: 2018; Vol. *29*.
(59) Tran, R.; Xu, Z.; Radhakrishnan, B.; Winston, D.; Sun, W.; Persson, K. A.; Ong, S. P. Surface energies of elemental crystals. *Sci. Data* **2016**, *3*, 1−13.
(60) Choi, Y. K.; Park, S. J.; Park, S.; Kim, S.; Kern, N. R.; Lee, J.; Im, W. CHARMM-GUI Polymer Builder for Modeling and Simulation of Synthetic Polymers. *J. Chem. Theory Comput.* **2021**, *17*, 2431−2443.

https://doi.org/10.1021/acs.jctc.1c00996
J. Chem. Theory Comput. 2022, 18, 479−493

(61) Essmann, U.; Perera, L.; Berkowitz, M. L.; Darden, T.; Lee, H.; Pedersen, L. G. A smooth particle mesh Ewald method. *J. Chem. Phys.* **1995**, *103*, 8577−8593.
(62) Ryckaert, J.-P.; Ciccotti, G.; Berendsen, H. J. C. Numerical integration of the cartesian equations of motion of a system with constraints: molecular dynamics of n-alkanes. *J. Comput. Phys.* **1977**, *23*, 327−341.
(63) Hess, B.; Bekker, H.; Berendsen, H. J.; Fraaije, J. G. LINCS: a linear constraint solver for molecular simulations. *J. Comput. Chem.* **1997**, *18*, 1463−1472.
(64) Lee, J.; Hitzenberger, M.; Rieger, M.; Kern, N. R.; Zacharias, M.; Im, W. CHARMM-GUI supports the Amber force fields. *J. Chem. Phys.* **2020**, *153*, No. 035103.
(65) Wulff, G., XXV Zur Frage der Geschwindigkeit des Wachsthums und der Auflösung der Krystallflächen. *Z. Kristallogr. - Cryst. Mater.* **1901**, *34*, 449−530.
(66) Murray, H. H. Overview — clay mineral applications. *Appl. Clay Sci.* **1991**, *5*, 379−395.
(67) Massaro, M.; Colletti, C. G.; Lazzara, G.; Riela, S. The Use of Some Clay Minerals as Natural Resources for Drug Carrier Applications. *J. Funct. Biomater.* **2018**, *9*, 58.
(68) Teich-McGoldrick, S. L.; Greathouse, J. A.; Cygan, R. T. Molecular dynamics simulations of structural and mechanical properties of muscovite: pressure and temperature effects. *J. Phys. Chem. C* **2012**, *116*, 15099−15107.
(69) Teich-McGoldrick, S. L.; Greathouse, J. A.; Cygan, R. T. Molecular Dynamics Simulations of Structural and Mechanical Properties of Muscovite: Pressure and Temperature Effects. *J. Phys. Chem. C* **2012**, *116*, 15099−15107.
(70) Hoffmann, F.; Cornelius, M.; Morell, J.; Froba, M. Silica-based mesoporous organic-inorganic hybrid materials. *Angew. Chem., Int. Ed.* **2006**, *45*, 3216−51.
(71) Slowing, I. I.; Trewyn, B. G.; Giri, S.; Lin, V. S. Y. Mesoporous Silica Nanoparticles for Drug Delivery and Biosensing Applications. *Adv. Funct. Mater.* **2007**, *17*, 1225−1236.
(72) Hassanali, A. A.; Zhang, H.; Knight, C.; Shin, Y. K.; Singer, S. J. The Dissociated Amorphous Silica Surface: Model Development and Evaluation. *J. Chem. Theory Comput.* **2010**, *6*, 3456−71.
(73) Lopes, P. E.; Murashov, V.; Tazi, M.; Demchuk, E.; Mackerell, A. D. Jr., Development of an empirical force field for silica. Application to the quartz-water interface. *J. Phys. Chem. B* **2006**, *110*, 2782−92.
(74) Goumans, T. P.; Wander, A.; Brown, W. A.; Catlow, C. R. Structure and stability of the (001) alpha-quartz surface. *Phys. Chem. Chem. Phys.* **2007**, *9*, 2146−52.
(75) Lamb, R. N.; Furlong, D. N. Controlled wettability of quartz surfaces. *J. Chem. Soc., Faraday Trans. 1* **1982**, *78*, 61.
(76) Gajjeraman, S.; Narayanan, K.; Hao, J.; Qin, C.; George, A. Matrix macromolecules in hard tissues control the nucleation and hierarchical assembly of hydroxyapatite. *J. Biol. Chem.* **2007**, *282*, 1193−204.
(77) Liao, C.; Xie, Y.; Zhou, J. Computer simulations of fibronectin adsorption on hydroxyapatite surfaces. *RSC Adv.* **2014**, *4*, 15759−15769.
(78) Schneider, C.; Glazov, M. M.; Korn, T.; Hofling, S.; Urbaszek, B. Two-dimensional semiconductors in the regime of strong light-matter coupling. *Nat. Commun.* **2018**, *9*, 2695.
(79) Wen, M.; Shirodkar, S. N.; Plecháč, P.; Kaxiras, E.; Elliott, R. S.; Tadmor, E. B. A force-matching Stillinger-Weber potential for MoS2: Parameterization and Fisher information theory based sensitivity analysis. *J. Appl. Phys.* **2017**, *122*, 244301.
(80) Jo, S.; Cheng, X.; Islam, S. M.; Huang, L.; Rui, H.; Zhu, A.; Lee, H. S.; Qi, Y.; Han, W.; Vanommeslaeghe, K.; MacKerell, A. D., Jr.; Roux, B.; Im, W. CHARMM-GUI PDB manipulator for advanced modeling and simulations of proteins containing nonstandard residues. *Adv. Protein Chem. Struct. Biol.* **2014**, *96*, 235−65.
(81) Ramezani-Dakhel, H.; Ruan, L.; Huang, Y.; Heinz, H. Molecular Mechanism of Specific Recognition of Cubic Pt Nanocrystals by Peptides and of the Concentration-Dependent Formation from Seed Crystals. *Adv. Funct. Mater.* **2015**, *25*, 1374−1384.
(82) Main, A. L.; Harvey, T. S.; Baron, M.; Boyd, J.; Campbell, I. D. The three-dimensional structure of the tenth type III module of fibronectin: An insight into RGD-mediated interactions. *Cell* **1992**, *71*, 671−678.
(83) Petrie, T. A.; Reyes, C. D.; Burns, K. L.; Garcia, A. J. Simple application of fibronectin-mimetic coating enhances osseointegration of titanium implants. *J. Cell. Mol. Med.* **2009**, *13*, 2602−2612.
(84) Richter, R. P.; Bérat, R.; Brisson, A. R. Formation of solid-supported lipid bilayers: an integrated view. *Langmuir* **2006**, *22*, 3497−3505.
(85) Chun, M. J.; Choi, Y. K.; Ahn, D. J. Formation of nanopores in DiynePC−DPPC complex lipid bilayers triggered by on-demand photo-polymerization. *RSC Adv.* **2018**, *8*, 27988−27994.
(86) Richter, R. P.; Brisson, A. R. Following the formation of supported lipid bilayers on mica: a study combining AFM, QCM-D, and ellipsometry. *Biophys. J.* **2005**, *88*, 3422−3433.
(87) Wu, E. L.; Cheng, X.; Jo, S.; Rui, H.; Song, K. C.; Davila-Contreras, E. M.; Qi, Y.; Lee, J.; Monje-Galvan, V.; Venable, R. M.; Klauda, J. B.; Im, W. CHARMM-GUI Membrane Builder toward realistic biological membrane simulations. *J. Comput. Chem.* **2014**, *35*, 1997−2004.
(88) Jo, S.; Lim, J. B.; Klauda, J. B.; Im, W. CHARMM-GUI Membrane Builder for mixed bilayers and its application to yeast membranes. *Biophys. J.* **2009**, *97*, 50−8.
(89) Jo, S.; Kim, T.; Im, W. Automated builder and database of protein/membrane complexes for molecular dynamics simulations. *PLoS One* **2007**, *2*, e880.
(90) Tadmor, E. B.; Elliott, R. S.; Sethna, J. P.; Miller, R. E.; Becker, C. A. The potential of atomistic simulations and the knowledgebase of interatomic models. *JOM* **2011**, *63*, 17−17.

https://doi.org/10.1021/acs.jctc.1c00996
J. Chem. Theory Comput. 2022, 18, 479−493